Concurrent optimisation of structural topology and fibre paths for 3D printing of continuous fibre composites based on chain primitive projection

Concurrent optimisation of structural topology and fibre paths for 3D printing of continuous fibre composites based on chain primitive projection

Shuai Wang[1,2], Jie Liu[1,*],Zhelong He[1], Dongmin Yang[2,**]

1. State Key Laboratory of Advanced Design and Manufacturing for Vehicle, College of Mechanical and Vehicle Engineering, Hunan University, Changsha 410082, China
2. Institute for Materials and Processes, School of Engineering, University of Edinburgh, Edinburgh, EH9 3FB, UK

Abstract

This study proposes a novel topology optimisation method based on the Geometry Projection Topology Optimisation method (GPTO) with the consideration of manufacturing constraints for the 3D printing of continuous fibre reinforced polymer composite structures. The proposed method uses connecting bars in chains to represent the continuous fibre filaments in the composite structure, as opposed to the use of separate bars as primitives. Thus, the method is termed as Chain Projection Topology Optimisation (CPTO), in which the chain-like primitives are equivalent to clusters of real printing paths. The 3D printing paths can be acquired by splitting the primitives evenly, which simplified the printing path design procedure to a great extent. In addition, manufacturing constraints can be easily imposed on the primitives, making it superior to density-based topology optimisation methods. An MBB beam, a cantilever beam, and a bridge case are optimised to demonstrate the CPTO's efficiency. It was found that the designs by CPTO possess comparable mechanical properties when compared to those by the Solid Orthotropic Material Penalization (SOMP) method while guaranteeing the composite structures are suitable for 3D printing and contain less microscopic defects in the printed fibre filaments.

Keywords: Topology optimisation; 3D printing; continuous fibre reinforced polymer composite; printing path planning.

1. Introduction

Fibre reinforced polymer (FRP) composites, including carbon fibre reinforced polymer (CFRP) composites and glass fibre reinforced polymer (GFRP) composites, have been widely used in aerospace, automotive and renewable energy industries over the past few decades. Numerous manufacturing

* Corresponding author. Email: liujie@hnu.edu.cn

** Corresponding author. Email: Dongmin.Yang@ed.ac.uk

methods have been developed to produce FRP composite products [1]. In some specific circumstances, lightweight composite structures with complex geometry are needed, where cutting and/or drilling processes are usually adopted to machine the composites. The machining process could lead to fibre breakage, interlayer delamination and/or matrix decomposition, thus deteriorating the mechanical performance of the composites [2-5]. With the recent rapid development of additive manufacturing (AM, also known as 3D printing) techniques, continuous fibre reinforced polymer composites can be directly printed by depositing composite filament to form 3D shapes and geometries [6-8], which provides a potential solution to manufacturing complex composite structures while eliminating or mitigating the manufacturing defects mentioned above.

Moreover, 3D printing could be combined with topology optimisation for lightweighting of composite structures. Several topology optimisation methods for FRP composites have been proposed in literature. Jia *et al*. [9] concurrently optimised topology and fibre orientation using a density-based topology optimisation method. Nomura *et al*. [10] used Cartesian components rather than angles as variables to prevent local minima when optimising topology and fibre orientation. Liu *et al*. [11, 12] proposed a Discrete-Continuous Parameterisation (DCP) method in which Solid Isotropic Material Penalisation (SIMP) [13-15] and Discrete Material Optimisation (DMO) [16, 17] are merged. Jantos *et al*. [18] presented an approach for simultaneous optimisation of topology and material orientation with high smoothness. Moter *et al*. [19] proposed a concurrent optimisation method considering stress constraints.

However, the optimised FRP composite structure generated by the above methods cannot be directly 3D printed. This is due to the necessary slicing procedure, in which printing path planning methods are required to convert the geometry into a sequence of coordinates. Markforged® has released its efficient slicing system Eiger for composite 3D printing and various other printing path designing methods, such as the principal stress method [20-22], Equally Space (EQS) method [23, 24], Offset method [23, 24] and Load Dependent Path Planning (LPP) method [25], have been proposed. However, there still exist a number of challenges when combining them with topology optimisation: *Phenomenon 1*, the composite structure may be infilled by incomplete fibre reinforcement, possibly leading to resin-rich areas and consequently heavily reduced mechanical performance; *Phenomenon 2*, the printing paths may consist of multiple sharp corners, where fibres could be twisted, misaligned or even broken, resulting in severe

manufacturing defects; *Phenomenon 3*, the printed fibre paths may overlap with each other, leading to non-uniform layer thickness of the printed composite.

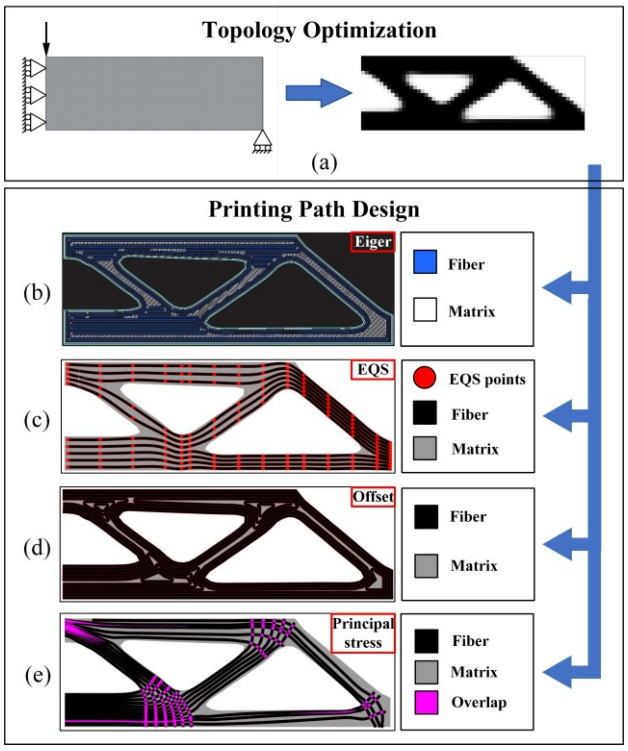

Fig. 1. (a) Topology optimisation using DCP [11] and printing paths designed by: (b) Markforged Eiger, (c) EQS method, (d) Offset method, and (e) Principal stress method

To further illustrate these challenging issues, the whole process of combining topology optimisation and printing path designing is shown in Fig. 1 using a Messerschmitt-Bölkow-Blohm (MBB) beam as an example. The structure is first optimised using the DCP method in Fig. 1(a), and the constitutive tensor of fibre reinforcement is adopted in every single element in this step. Then, different printing paths are generated by Eiger (a commercial software from Markforged®), EQS method, Offset method and principal stress method separately in Fig. 1(b-e). For the printing path designed by Eiger, an apparent discrepancy exists between the printing paths and the original topology optimisation result as a large amount of matrix is infilled in instead of fibre filaments, which can be categorised as *Phenomenon 1*. The same issue occurs in other three illustrated methods, but compared with Eiger, the paths designed by these methods generally coincide with the topology optimisation result. According to [24], both EQS and Offset methods result in incomplete infilling of the structure, with EQS generally yielding a lower infill rate than the Offset method. Furthermore, as shown in Fig. 1(d), sharp corners exist in many loop-like paths. According to [26] and [27], when the fibre filaments are printed with a large curvature, the fibres

will inevitably suffer from twisting, folding, misalignment and even breakage, and deteriorate the mechanical performance of the composite structure accordingly. Thus, the existence of sharp corners is categorized as *Phenomenon 2*. It should be noted that some major modifications of Offset printing paths are needed to connect the loop-like paths, which could introduce undesirable manual factors [24]. Moreover, researchers have conducted topology optimisation considering overlap constraints such that the adjacent fibre filaments do not overlap with each other during the printing. Among those methods, the Level-set method [28, 29] was most commonly used, in which the printing paths were generated by extracting iso-value level set contours [30-32]; thus, it inevitably generates loop-like printing paths and introduces the same problem as for the Offset method. The printing fibre paths may also be designed along the principal stress trajectories to improve the structural stiffness [22, 33, 34]. However, undesirable path cross-overs are inevitable. As illustrated in Fig. 1(e), the area in purple represents the overlaps between fibre filaments printed along the principal stress trajectories. According to [35], the presence of overlap between two different layers will result in fibre-rich regions, thus causing the local increase of thickness. Such a phenomenon is especially undesirable during carbon fibre 3D printing because the thickness increase at the overlap positions will impede the movement of the printing nozzle. The undesirable phenomenon depicted above is categorised as *Phenomenon 3* in this study.. For a better understanding of this study, all the undesirable phenomena in continuous fibre 3D printing path design are listed in Table 1.

Table 1 Undesirable phenomena in continuous fibre 3D printing path design

Name	Manifestation
Phenomenon 1	The structures are infilled not according to the material used in the topology optimisation
Phenomenon 2	The printing path is composed of loops and/or sharp corners
Phenomenon 3	The printing paths overlap with each other

According to the above literature survey, the existing 3D printing path planning methods are not capable of generating fully infilled paths without sharp corners and overlaps for the topology-optimised continuous FRP composite structures. The fundamental reason for this challenge is that the traditional density-based topology optimisation and 3D printing path planning are conducted separately, which means that during the topology optimisation, the voxels are optimised, but the geometry requirements for the path planning are not fully considered. Thus, the final design of printing paths conflicts with the

optimisation result in most situations. Topology optimisation and path planning are highly integrated for the Level-set method, and the generated paths are consistent with the optimisation result. However, optimisation constraints still need to be proposed to eliminate closed loops in the paths. Consequently, the paths extracted from the Level-set function may not be manufacturable. In the authors' opinion, 3D printing path planning for continuous FRP composite structures is a geometry-related problem which would be better solved at the geometry level during topology optimisation.

In 2015, Norato *et al*. proposed the Geometry Projection Topology Optimisation (GPTO) method for isotropic materials [36, 37]. In GPTO, the bar-like geometry primitives are arranged at the geometry level and then projected onto fixed meshes for finite element analysis (FEA). The position, width, and existence of each primitive are optimised according to the gradient information of the optimisation problem. The GPTO method dramatically reduces the number of optimisation variables and efficiently converges in 2D and 3D cases. More importantly, the method is based on simple geometric primitives, which makes it easy to constrain the geometric profile when performing topology optimisation.

Though Smith and Norato [38, 39] extended the GPTO method to fibre-reinforced bars and plates in their recent studies, the newly proposed methods are not targeted at 3D printing, which means that the printing paths cannot be generated directly after topology optimisation. It is also worth noting that Greifenstein *et al*. [40] proposed a spline-based geometry projection method to optimise fibre reinforced composite structures. In their research, the constraint of spline primitive curvature was considered, but a printing path planning method was still needed to convert the optimised structures into printing paths. Hence, the GPTO method and its derivatives must be combined with printing path planning algorithms when designing the 3D printed structures, making GPTO face the same issues as of the density-based topology optimisation methods.

Therefore, this study proposes a novel simultaneous structural topology and printing path optimisation method based on the GPTO method. Instead of using bars as geometry primitives, chains constituted by bars are adopted in this study, thus it is called Chain Projection Topology Optimisation (CPTO) method. By using chains as geometry primitives and constraining their widths to be integral multiples of the width of the printed fibre filament, the CPTO method ensures that printing paths can be generated along the orientation of chains without additional processing. The proposed approach makes printing paths directly in accord with the optimised topology, resulting in a smoother and more efficient manufacturing process.

Furthermore, constraints such as overlaps and maximum allowable turning angles of printing paths can be easily introduced to the optimisation. The rest of the paper is arranged as follows. In Section 2, the theory and implementation of the CPTO method is introduced. Numerical examples are then presented in Section 3 to illustrate the effectiveness of the CPTO method. Besides, two samples of different printing paths for the same continuous CFRP composite structure are printed out to demonstrate the compatibility of the method for actual 3D printing. The main conclusions of this study are drawn in Section 4.

2. Methodology of Chain Projection Topology Optimisation

The fundamental of the CPTO method is that the geometry is arranged with pre-designed chain-like primitives at a higher level, which is then converted into a pseudo-density field and assembled on a fixed mesh for FEA. Several manufacturing constraints are imposed due to continuous fibre 3D printing characteristics. Instead of merging geometry primitives using the *p*-norm or Kreisselmeier–Steinhauser (KS) function, density fields of different primitives are accumulated so that the filament overlap issue can be avoided by constraining the density value. Moreover, the angle between two adjacent bars in the same chain is constrained to prevent the sharp corners of the printing paths. Most importantly, the widths of chains are set to integer multiples of the filament; thus, the topology of chains can be directly converted into printing paths. More detailed explanations are presented below.

2.1 Chain-like primitive modeling

By connecting the bars end to end, primitives with chain geometries are formed. Suppose that n chain primitives exist in the design space, and each chain consists of m bar-shaped components. Each chain is defined by the coordinates of control points and the width of the chain. In

Fig. 2, a chain consisting of 4 bars is illustrated. i represents the serial number of the primitive, thus $w_{c(i)}$ denotes the width of *i*th chain primitive and $x_{i,3}$ denotes the coordinate of 3rd control point in *i*th chain primitive.

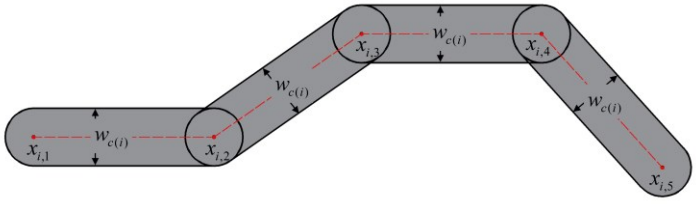

Fig. 2. Chain-like primitive in CPTO

The projected density field of the chains is calculated in the first step as given in [37]

$$\rho_{c(i)}\left(\frac{l_{c(i)}}{r_e}\right)=\begin{cases}0 & \text{if } l_{c(i)}/r_e>1\\ H\left(l_{c(i)}/r_e\right) & \text{if } \left|l_{c(i)}/r_e\right| \le 1\\ 1 & \text{if } l_{c(i)}/r_e<-1\end{cases} \tag{1}$$

in which

$$H(x)=1-\frac{\arccos(x)+x\sqrt{1-x^2}}{\pi} \tag{2}$$

and $\rho_{c(i)}$ denotes the projected density field of *i*th chain, l_i is the distance from the element centroid to *i*th chain's boundary, x_e is the coordinate of the element centroid, $\boldsymbol{x}_i$ are the coordinates of all the control points of *i*th chain. Eq. (1) and Eq. (2) calculate the intersection area between the chain primitive and the circle of radius r_e located at the centroid of the element, as illustrated in Fig. 3.

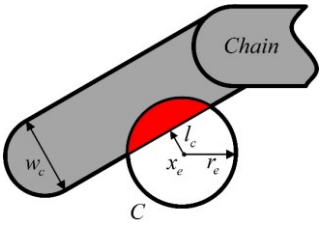

Fig. 3. Computing the intersection area

The distance l_i can be calculated by

$$l_{c(i)}=\left(\sum_{j=1}^{m}\left(\frac{1}{d_{i,j}+\varepsilon_d}\right)^{p_d}\right)^{-\frac{1}{p_d}}-\frac{w_{c(i)}}{2} \tag{3}$$

where $d_{i,j}$ is the distance from the element to the medial axis of *j*th bar which composes *i*th chain, ε_d is a rather small value to prevent singularity, and p_d is the penalisation factor of the *p*-norm function taken as 15 in this study. It is noteworthy that Eq. (3) acts as a differentiable 'min' function.

Fig. 4 shows the procedure of transformation from several $d_{i,j}$ to a single l_c.

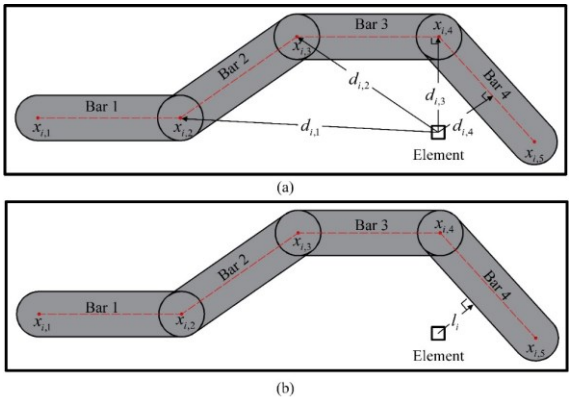

Fig. 4. Schematic diagrams to calculate (a) the distance between the element and bars and (b) l_i with the minimum function in Eq. (3)

The calculation of $d_{i,j}$ depends on the relative position between the element and the bar primitive [36], which can be summarized into three scenarios, as shown in Fig. 5:

$$d_{i,j} = \begin{cases} \|v_{b1-e}\| & \text{if } L_{be} \le 0 \\ \|v_{b2-e}\| & \text{if } L_{be} \ge L_b \\ d_{be} & \text{else} \end{cases} \tag{4}$$

in which v_{b1-e} denotes the vector from the control point x_{b1} to the element, v_{b2-e} denotes the vector from the control point x_{b2} to the element, $\|\square\|$ denotes the computation of Euclidean distance, L_b is the distance from x_{b1} to x_{b2}, d_{be} and L_{be} are parallel and perpendicular components of v_{b1-e}, respectively.

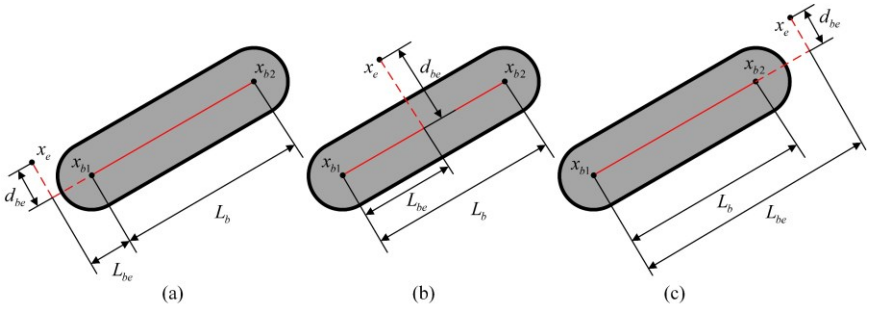

Fig. 5. Three scenarios when computing d_{bar} : (a) $L_{be} \le 0$, (b) $0 < L_{be} < L_b$, and (c) $L_{be} \ge L_b$

To alleviate the grayscale problem on the boundary of the chain primitives, the penalisation factor p_ρ is introduced. In this study, p_ρ is fixed to 3 to penalise the density field. The penalised density of *i*th chain primitive can be given by

$$\tilde{\rho}_{c(i)} = \rho_{c(i)}{}^{p_\rho} \tag{5}$$

The outline of the *i*th chain primitive is given in Fig. 6(a), $\varphi_{i,1}\sim\varphi_{i,4}$ are the relative rotation angles of each bar component with respect to the global coordinate system. The distribution of the chain's $\tilde{\rho}_{c(i)}$ field is illustrated in Fig. 6(b). Since the fibre reinforcement is treated as orthotropic material in this study, the constitutive matrix of the elements surrounding/inside *i*th chain primitive can be described by

$$C_i = \tilde{\rho}_{c(i)} T^T(\varphi_{c(i)}) C_f T(\varphi_{c(i)}) \tag{6}$$

in which C_f is the constitutive matrix of fibre reinforcement, $T(\varphi)$ is the transform matrix which can be given as

$$T(\varphi) = \begin{bmatrix} \cos^2\varphi & \sin^2\varphi & \sin\varphi\cos\varphi \\ \sin^2\varphi & \cos^2\varphi & -\sin\varphi\cos\varphi \\ -2\sin\varphi\cos\varphi & 2\sin\varphi\cos\varphi & \cos^2\varphi-\sin^2\varphi \end{bmatrix} \tag{7}$$

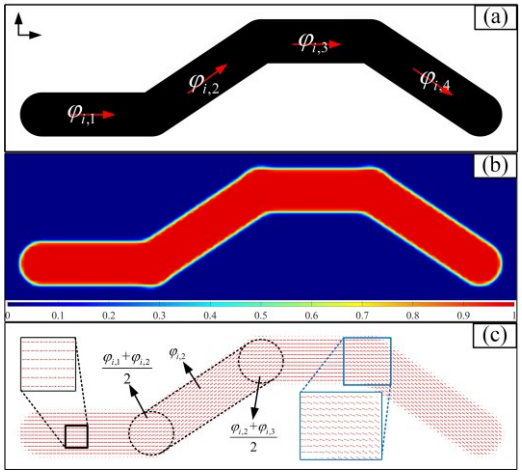

Fig. 6. (a) The layout of a given chain primitive, (b) the corresponding distribution of $\tilde{\rho}_c$ and (c) the orientation of the elements enclosed by the chain primitive

$\varphi_{c(i)}$ denotes the orientation field defined by *i*th chain primitive, which is computed by

$$\varphi_{c(i)} = \frac{\sum_{j=1}^{m}\left(\rho_{i,j}\varphi_{i,j}\right)}{\sum_{j=1}^{m}\rho_{i,j} + \varepsilon} \tag{8}$$

where $\rho_{i,j}$ is the density field of *j*th bar component in *i*th chain primitive, ε is a relatively small value to prevent singularity. $\rho_{i,j}$ can be computed in the same way in [36]:

$$\rho_{i,j} = \begin{cases} 0 & \text{if } \dfrac{d_{i,j} - w_i/2}{r_e} > 1 \\ H\left(\dfrac{d_{i,j} - w_i/2}{r_e}\right) & \text{if } \left|\dfrac{d_{i,j} - w_i/2}{r_e}\right| \le 1 \\ 1 & \text{if } \dfrac{d_{i,j} - w_i/2}{r_e} < -1 \end{cases} \tag{9}$$

By Eq.(8) and Eq.(9), the orientation of the chain primitives is projected to the elements for FEA. The orientation field $\varphi_{c(i)}$ is illustrated in Fig. 6(c). It can be noticed that the orientation within the black-boxed area is consistent and aligned with the placement direction of the corresponding bar-shaped component. On the other hand, the elements within the blue-boxed area are located at the connection points of the bars, and the orientation of these units is the average value between the orientations of the two bars.

Eq.(6) gives the way to compute the constitutive matrix of the elements which are inside the chain primitive, but unable to cover the area where $\tilde{\rho}_{c(i)}=0$. Thus, this study adopts a double-material model with a Sigmoid function to enable the optimisation of the matrix material and the fibre reinforcement. With the density field ρ_e, the matrices of all elements can be calculated by

$$C_e = \sum_{i=1}^{n} \tilde{\rho}_{c(i)} T^T(\varphi_{c(i)}) C_f T(\varphi_{c(i)}) + \frac{1}{1 + e^{t(\sum_{i=1}^{n} -\tilde{\rho}_{c(i)} + a)}} C_m \tag{10}$$

In Eq. (10), t and a are parameters of the Sigmoid function, in this study, $t = -100$ and $a = 0.06$. C_m is the constitutive matrix of a given isotropic material. The Sigmoid function works as a 'selector' which assigns constitutive matrices to elements (*i.e.*, when $\sum \tilde{\rho}_{c(i)} = 0$, which means that the element is not covered by any chain primitive, C_m is assigned to the element). It is worth noting that C_m can represent the stiffness matrix of any isotropic material such that when C_m is set to zero, a structure composed of fibre reinforcement and voids can be obtained. On the other hand, when C_m is set to the constitutive matrix of a polymer, the final design will be composed of fibre reinforcement and the polymer .

2.2 Manufacturing constraints

Since CPTO is intended for the design of FRP composite structures and the generation of printing paths directly along the orientations of chain primitives, thus manufacturing constraints should be specifically considered to avoid printing path overlaps and sharp corners of printed fibre filaments. According to the descriptions above, $\rho_{c(i)}$ is the pseudo-density field defined by the distances from elements to the chain primitive. Let ρ_e be the summation of all the density field $\rho_{c(i)}$:

$$\rho_e = \sum_{i=1}^{n} \rho_{c(i)} \tag{11}$$

The value of $\rho_{c(i)}$ field for each element locates in $[0,1]$. It is easy to find that when a chain primitive overlaps with others, for the elements in the overlap area, we will have $\rho_e \geq 2$, which means that the overlaps of fibre reinforcements (*Phenomenon 3*) can be avoided by constraining the value of ρ_e.

An illustration of two overlapped chain primitives is given in Fig. 7. It is easy to find that the overlap areas of two different primitives are detected by highlighting the area in which ρ_e=2. However, it is important to note that ρ_e is a field composed of N values (N denotes the total number of elements). To avoid primitive overlaps in the whole design domain, theoretically, N constraint functions should be built, which would cause a convergence issue for the optimisation. To address this, the *p*-mean of ρ_e, which is continuously differentiable, is adopted here, reading

$$\rho_e^{\max} = \left(\frac{1}{N} \sum_{i=1}^{N} {\rho_{e(i)}}^{p_e} \right)^{\frac{1}{p_e}} \tag{12}$$

where N is the total number of elements, $\rho_{e(i)}$ denotes the corresponding ρ_e value for *i*th element, and p_e is the power index taken as 15 for the balance of accuracy and convergence.

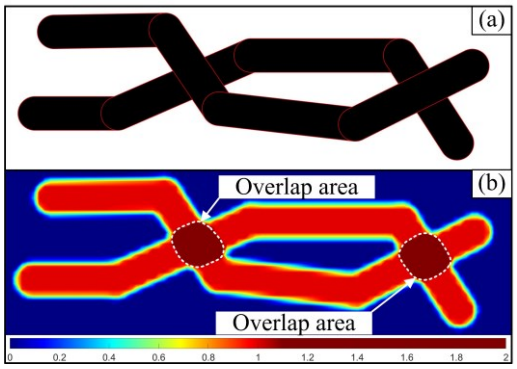

Fig. 7. (a) Geometry of two chain primitives; (b) The distribution of field ρ_e and the overlap areas.

The proposed method is able to achieve simultaneous design of topology and printing paths by dividing the chain primitives evenly. As shown in Fig. 8, $w_{c(i)}$ is the width of the given chain primitive, w_f is the width of the printed fibre filament. It could be seen that by constraining the value of $w_{c(i)}$, ensuring that it is always approximately equal to a specific integer multiple of w_f during the optimisation process, the equivalent relationship between the geometric component and the printing path can be achieved. The constraint can be given as:

$$w_{c(i)} \in \left[\lambda w_f - \eta, \lambda w_f + \eta\right] \tag{13}$$

where λ is the number of filaments contained in each chain component, which is given as an integer before the optimisation begins, η is a relatively small value to facilitate the convergence of the optimisation.

More importantly, due to the compact arrangement of the printing paths, the chain primitives are fully infilled by the fibre filaments, which means that the structure will be infilled by the correct material as it should be, indicating that *Phenomenon 1* is prevented.

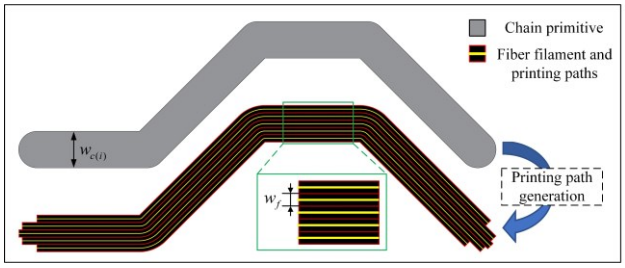

Fig. 8. Printing path generation and the constraints on the widths of chain primitives

Last but not least, it is well known that fibre breakage and twisting may occur within the printing paths with relatively large curvatures, thus deteriorating the mechanical properties of the printed composite structure [41, 42]. Therefore, besides the overlap constraint, angles between adjacent bars in every chain primitive are constrained to avoid sharp corners (*e.g.* <90°) in printing paths to minimise the fibre damage.

As shown in Fig. 9, the angles between two adjacent bars can be given by

$$\theta = \arccos\left(\frac{V_1 \cdot V_2}{\|V_1\|\|V_2\|}\right) \tag{14}$$

in which $V_1 = (x_2 - x_1, y_2 - y_1)$ and $V_2 = (x_3 - x_2, y_3 - y_2)$, $\|\square\|$ is the 2-norm operator.

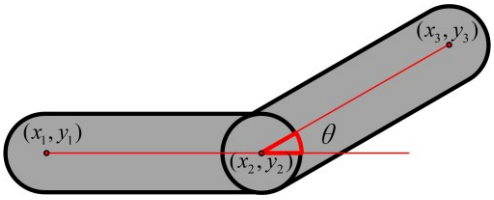

Fig. 9. The angle between two adjacent bars

2.3 Optimisation problem

The compliance optimisation problem for CPTO can be defined as

$$\begin{aligned}
&\text{find}: x, w_c \\
&\min: c = U^T K U = \sum_{i=1}^{N} u_e^T K_e u_e \\
&\text{subject to}: V_f = \left(\sum_{i=1}^{N} \rho_{c(i)} V_e\right) / V_0 \le f \\
&\quad KU = F \\
&\quad \rho_e^{\max} \le \rho_e^{\lim}, \\
&\quad w_{c(i)} \in [\lambda w_f - \eta, \lambda w_f + \eta], \quad i = 1, \cdots, n, \\
&\quad x_{i,j} \in \Omega, \quad i = 1, \cdots, n, \\
&\qquad\qquad\qquad\quad j = 1, \cdots, m+1, \\
&\quad \theta_{i,j} \le \theta_{\lim}, \quad i = 1, \cdots, n, \\
&\qquad\qquad\qquad\quad j = 1, \cdots, m-1,
\end{aligned} \tag{15}$$

where c is the compliance, U and F are the vectors of displacement and force respectively, K is the global stiffness matrix, N is the total number of elements, u_e is the displacement vector of the element, K_e is the stiffness matrix of elements, V_e is the volume of a single element, V_0 is the volume of the whole design area, f is the prescribed volume fraction limitation, n is the number of chain

primitives, m is the number of bars in a chain primitive, $\rho_e^{\lim}$ is the limitation value for $\rho_e^{\max}$, and $\theta_{\lim}$ is the limitation value for the angles ($\theta_{\lim} = \pi / 2$ in this study).

The computation of K_e can be given in a Gauss quadrature manner:

$$K_e = \iint B^T C_e B d\Omega \approx \sum_{i=1}^{n_{gp}} \sum_{j=1}^{n_{gp}} \left(W_i W_j B^T C_e B |J| \right) \tag{16}$$

where n_{gp} is the number of Gauss points, B is the strain-displacement matrix, J is the Jacobian matrix, and C_e is the constitutive matrix acquired by Eq. (10).

2.4 Sensitivity analysis

This study adopts the globally convergent method of moving asymptotes (GCMMA) algorithm [43] to solve the optimisation problem efficiently. The required analytical sensitivities are presented in this section. Since the variables are composed of the coordinates of control points x and the widths of chain primitives w_c, the sensitivity of optimisation target c can be given by:

$$\frac{\partial c}{\partial x} = \sum_{i=1}^{n} \frac{\partial c}{\partial \tilde{\rho}_{c(i)}} \frac{\partial \tilde{\rho}_{c(i)}}{\partial \rho_{c(i)}} \frac{\partial \rho_{c(i)}}{\partial x} + \sum_{i=1}^{n} \left[\frac{\partial c}{\partial \varphi_{c(i)}} \left(\sum_{j=1}^{m} \frac{\partial \varphi_{c(i)}}{\partial \rho_{i,j}} \frac{\partial \rho_{i,j}}{\partial x} + \sum_{j=1}^{m} \frac{\partial \varphi_{c(i)}}{\partial \rho_{i,j}} \frac{\partial \varphi_{i,j}}{\partial x} \right) \right] \tag{17}$$

$$\frac{\partial c}{\partial w_c} = \sum_{i=1}^{n} \frac{\partial c}{\partial \tilde{\rho}_{c(i)}} \frac{\partial \tilde{\rho}_{c(i)}}{\partial \rho_{c(i)}} \frac{\partial \rho_{c(i)}}{\partial w_c} + \sum_{i=1}^{n} \left[\frac{\partial c}{\partial \varphi_{c(i)}} \left(\sum_{j=1}^{m} \frac{\partial \varphi_{c(i)}}{\partial \rho_{i,j}} \frac{\partial \rho_{i,j}}{\partial w_c} \right) \right] \tag{18}$$

in which

$$\frac{\partial c}{\partial \tilde{\rho}_{c(i)}} = -u_e^T \left(\sum_{j=1}^{n_{gp}} \sum_{k=1}^{n_{gp}} W_j W_k B^T \frac{\partial C_e}{\partial \tilde{\rho}_{c(i)}} B |J| \right) u_e \tag{19}$$

$$\frac{\partial C_e}{\partial \tilde{\rho}_{c(i)}} = T^T(\varphi_{c(i)}) C_f T(\varphi_{c(i)}) - \frac{t e^{t(\sum \tilde{\rho}_{c(i)} + a)}}{(1 + e^{t(\sum \tilde{\rho}_{c(i)} + a)})^2} C_m \tag{20}$$

$$\frac{\partial \tilde{\rho}_{c(i)}}{\partial \rho_{c(i)}} = p_\rho {\rho_{c(i)}}^{p_\rho - 1} \tag{21}$$

$$\frac{\partial \rho_{c(i)}}{\partial x} = \frac{\partial \rho_{c(i)}}{\partial l_{c(i)}} \frac{\partial l_{c(i)}}{\partial d_{i,j}} \frac{\partial d_{i,j}}{\partial x} \tag{22}$$

$$\frac{\partial \rho_{c(i)}}{\partial w_{c(i)}} = \frac{\partial \rho_{c(i)}}{\partial l_{c(i)}} \frac{\partial l_{c(i)}}{\partial w_{c(i)}} \tag{23}$$

$$\frac{\partial \rho_{c(i)}}{\partial l_{c(i)}} = \begin{cases} \dfrac{2l_{c(i)}^2}{\pi r_e^2 \sqrt{r_e^2 - l_{c(i)}^2}} & \text{if } \left|\dfrac{l_{c(i)}}{r_e}\right| \le 1 \\ 0 & \text{else} \end{cases} \tag{24}$$

$$\frac{\partial l_{c(i)}}{\partial d_{i,j}} = \left(\sum_{k=1}^{m} \left(\frac{1}{d_{i,k} + \varepsilon_d} \right)^{p_d} \right)^{\frac{1}{p_d}-1} \cdot \left(\frac{1}{d_{i,j} + \varepsilon_d} \right)^{p_d+1} \tag{25}$$

The sensitivity of the distance $d_{i,j}$ with respect to the control points of the bar component x_{b1} and x_{b2} is the same as the one in [37]:

$$\frac{\partial d_{i,j}}{\partial x_{bs}} = \frac{1}{d_{i,j}} \begin{cases} -v_{b1-e}\delta_1^s & \text{if } L_{be} \le 0 \\ -v_{b2-e}\delta_2^s & \text{if } L_{be} > L_b \\ -r_e\left(\delta_1^s + \dfrac{L_{be}}{L_b}\left(\delta_2^s - \delta_1^s \right) \right) & \text{otherwise} \end{cases} \tag{26}$$

in which $s \in \{1,2\}$ is the index of the car component's control points, δ_k^s is the Kronecker delta.

$$\frac{\partial c}{\partial \varphi_{c(i)}} = -u_e^T \left(\sum_{j=1}^{n_{gp}} \sum_{k=1}^{n_{gp}} W_j W_k B^T \frac{\partial C_e}{\partial \varphi_{c(i)}} B \left| J \right| \right) u_e \tag{27}$$

$$\frac{\partial C_e}{\partial \varphi_{c(i)}} = \tilde{\rho}_{c(i)} \left[\frac{\partial T^T(\varphi_{c(i)})}{\partial \varphi_{c(i)}} C_f T(\varphi_{c(i)}) + T^T(\varphi_{c(i)}) C_f \frac{\partial T(\varphi_{c(i)})}{\partial \varphi_{c(i)}} \right] \tag{28}$$

$$\frac{\partial \varphi_{c(i)}}{\partial \rho_{i,j}} = \frac{\left(\sum_{j=1}^{m} \rho_{i,j} + \varepsilon \right) \varphi_{i,j} - \sum_{j=1}^{m} \rho_{i,j} \varphi_{i,j}}{\left(\sum_{j=1}^{m} \rho_{i,j} + \varepsilon \right)^2} \tag{29}$$

$$\frac{\partial \varphi_{c(i)}}{\partial \varphi_{i,j}} = \frac{\rho_{i,j}}{\sum_{j=1}^{m} \rho_{i,j} + \varepsilon} \tag{30}$$

The sensitivity of the volume fraction is computed by:

$$\frac{\partial V_f}{\partial x} = \sum_{i=1}^{n} \frac{\partial V_f}{\partial \rho_{c(i)}} \frac{\partial \rho_{c(i)}}{\partial x} \tag{31}$$

$$\frac{\partial V_f}{\partial w_{c(i)}} = \frac{\partial V_f}{\partial \rho_{c(i)}} \frac{\partial \rho_{c(i)}}{\partial w_{c(i)}} \tag{32}$$

The sensitivity of the overlap constraint can be given by:

$$\frac{\partial \rho_e^{\max}}{\partial x} = \frac{\partial \rho_e^{\max}}{\partial \rho_e} \left(\sum_{i=1}^{n} \frac{\partial \rho_e}{\partial \rho_{c(i)}} \frac{\partial \rho_{c(i)}}{\partial x} \right) \tag{33}$$

$$\frac{\partial \rho_e^{\max}}{\partial w_{c(i)}} = \frac{\partial \rho_e^{\max}}{\partial \rho_e} \frac{\partial \rho_e}{\partial \rho_{c(i)}} \frac{\partial \rho_{c(i)}}{\partial w_{c(i)}} \tag{34}$$

The sensitivity analysis of the angle θ is given in Appendix A.

3. Numerical examples

In this section, an MBB case, a cantilever beam case, and a bridge case are presented to demonstrate the implementation of the CPTO method. In the MBB case and the cantilever case, the optimised structures are composed of two different materials: continuous carbon fibre reinforced epoxy (CCF/Epoxy) and Polyamide-6 (PA6). The composite structure designed by CPTO is compared with the traditional unidirectional (UD) composite to demonstrate the effectiveness of the proposed method. To investigate the performance of the CPTO method compared to the conventional sequential technique, bridge structures designed by CPTO and DCP+Offset (DCP for topology optimisation, Offset for printing path planning) are analysed and compared. The mechanical properties of the material used in the MBB and the cantilever cases are listed in Table 2.

Table 2. Mechanical properties of the materials in the MBB and cantilever case

Material	E_1 (GPa)	E_2 (GPa)	G (GPa)	v_{12}	v_{21}
Carbon fibre/Epoxy filament	139.50	5.94	2.17	0.3250	0.0138
PA6	1.70				0.30

3.1 MBB

The boundary and loading conditions of the MBB beam are given in Fig. 10(a), and a unidirectional carbon fibre composite modeled by the CPTO method is presented in Fig. 10(b). The volume fraction of carbon fibre filaments is 0.5. The compliance of the UD structure is 108.03. The UD structure is set as the benchmark in this case study.

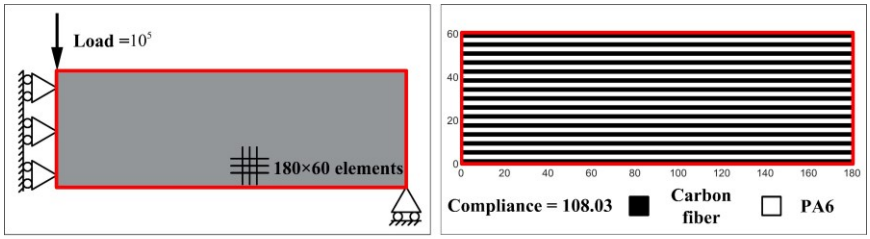

Fig. 10. (a) Boundary and loading conditions of MBB beam, and (b) UD structure composed of carbon fibre and PA6.

In Fig. 11**Error! Reference source not found.**, topology optimisation is conducted using the CPTO method. Since the CPTO method is a geometry projection method, the number of chain primitives and the number of bars in each chain primitive would inevitably affect the optimisation results. Thus, three different chain primitive layouts are studied. The initial designs are given in Fig. 11**Error! Reference source not found.**(a1)-(a3). Fig. 11**Error! Reference source not found.**(a1) illustrates the initial design which contains three chain primitives. Each primitive is composed of four connected bars, and has five printed carbon fibre filaments in the width direction. For simplicity, the case is termed as "CPTO 3C4B". This rule of abbreviation is applied for all the following cases. More detailed information of the chain primitive layouts is listed in Table 3.

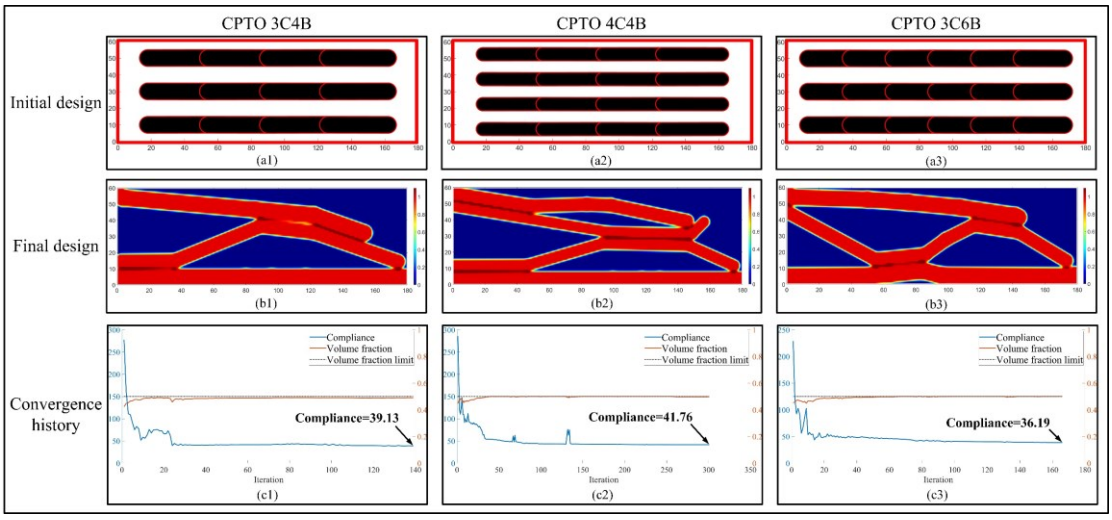

Fig. 11. Topology optimisation results of the MBB case

Table 3 The chain primitive layouts for the MBB case

Case	Number of chain primitives	Number of bar components in each chain
CPTO 3C4B	3	4
CPTO 4C4B	4	4

CPTO 3C6B	3	6

The distribution of ρ_e is illustrated in Fig. 11**Error! Reference source not found.**(b1)-(b3). It should be noted again that according to Eq. (10), the area where $\rho_e = 0$ is infilled with PA6. The area where $\rho_e = 1$ is infilled with carbon fibre and the area where $\rho_e > 1$ denotes the overlapped fibre filaments. It can be seen that overlaps of filaments barely exist, except in the contact regions between different chain primitives, which is acceptable for manufacturing as the areas are relatively small. Thus, it can be concluded that CPTO successfully prevents *Phenomenon 3* in the MBB case. The convergence history of the studied cases is given in Fig. 11**Error! Reference source not found.**(c1)-(c3). The optimisation stops when the iteration reaches 300, or the change of design variables falls below 10^{-4}. For CPTO 3C4B, the optimisation takes 139 iterations to converge. The compliance of the final design is 39.13. For CPTO 4C4B, the compliance of the final design is 41.76. It reaches the limitation of iteration for the algorithm to converge. And for CPTO 3C6B, it takes 166 iterations for the algorithm to complete the optimisation. The compliance of the final design is 36.19.

In order to prove the effectiveness of the CPTO method in printing path planning, the printing paths are drawn in Fig. 12**Error! Reference source not found.**. The printing paths for fibre filament are obtained by directly splitting the chain primitives evenly, as the widths of the primitives are approximately equal to the integral multiple of the width of printed fibre filament. The printing paths for infilling PA6 are generated by Ultimaker Cura®. Compared with the printing paths illustrated in Fig. 1, the carbon fibre filaments fully occupy the area for fibre reinforcement with no loop-like path, thus primarily facilitating the 3D printing process. From Fig. 12**Error! Reference source not found.**, it is easy to find that the area for carbon fibre filaments is fully infilled. With the enforcement of angle constraints in Eq. (15), no sharp corner exists in the carbon fibre printing paths, indicating that *Phenomenon 1* and *Phenomenon 2* are successfully prevented.

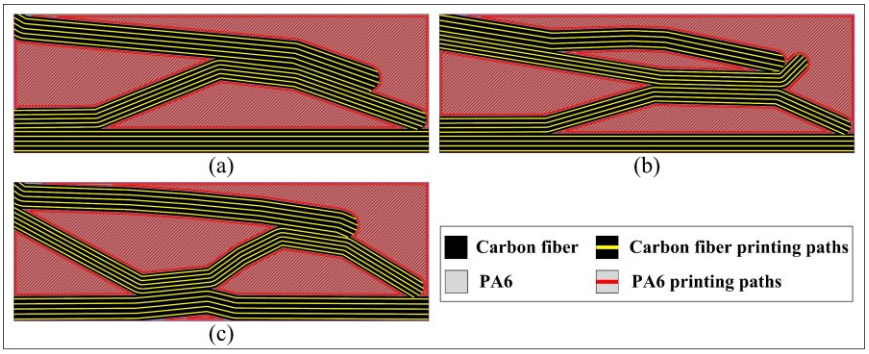

Fig. 12. Printing paths designed by the CPTO method

The comparison of the mechanical performance of all these cases is shown in Fig. 13. In Fig. 13, UD denotes the structure in Fig. 10(b). The y-axis of Fig. 13 represents the stiffness of each optimised structure, which is defined by

$$stiffness = \frac{1000}{compliance} \tag{35}$$

From Fig. 13, it can be seen that the optimisation results by the CPTO method perform much better than the UD composite structure, while the mechanical performance varies depending on the primitive number and the bar number in each chain primitive. It can be seen that, in this case, increasing the number of chain primitives leads to reduced stiffness, probably due to the constraint of chain primitive overlaps, which tends to lead each chain primitive to be confined to a relatively small area during optimisation to avoid intersecting with others. As long as one primitive is stabilized in the middle of the design domain, other primitives will be obstructed from freely moving across that region, thus likely preventing the algorithm from finding the optimal solution. On the other hand, the stiffness slightly increases when the chain primitive contains more bar components, which introduces more freedom to the algorithm to search for the optimal solution.

Meanwhile, to verify the effectiveness of the proposed method in the perspective of sensitivity analysis, a comparison of analytical sensitivity and finite difference (FD) check is given in Fig. 14. For the 3C4B MBB case, 33 variables (30 for control points positions and 3 for chain widths) are involved. From Fig.

14, it can be seen that the analytical sensitivity results coincide with the FD results, which indicates that the proposed method can accomplish the optimisation efficiently.

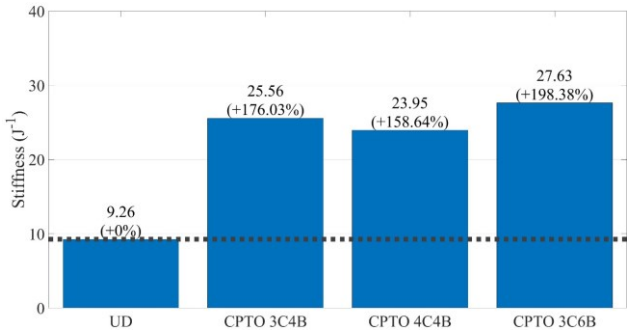

Fig. 13. Structural stiffness of MBB based on different design methods

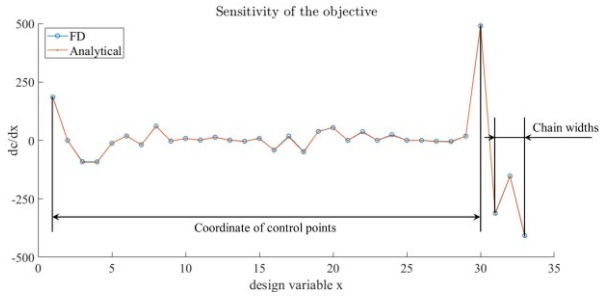

Fig. 14. Finite difference check of the objective function for the 3C4B MBB case

3.2 Cantilever

The second case is a cantilever with the left edge fixed and a vertical load applied at the top-right end, as illustrated in **Error! Reference source not found.**(a). Similar to the MBB case, a traditional UD composite structure is used as a benchmark, as shown in **Error! Reference source not found.**(b). The compliance of the UD structure is 63.10.

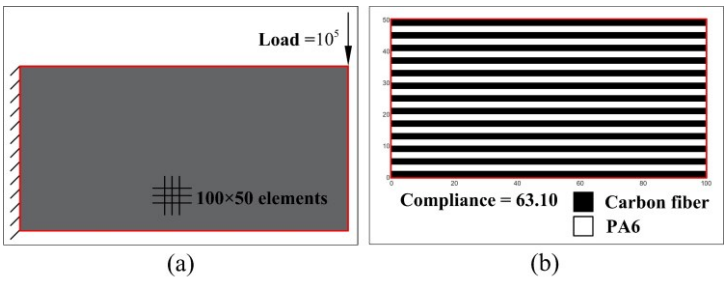

Fig. 15. (a) Boundary and loading conditions of the cantilever and (b) UD composite structure composed of carbon fibre filament and PA6.

In Fig. 16**Error! Reference source not found.Error! Reference source not found.**, topology optimisation of the cantilever is conducted using the CPTO method. Like the optimisation of the MBB beam, three different chain primitive layouts are studied. The initial designs are given in Fig. 16**Error!**

Reference source not found.Error! Reference source not found.(a1)-(a3). The information of the chain primitive arrangements is listed in Table 4.

The distribution of ρ_e is illustrated in Fig. 16**Error! Reference source not found.**(b1)-(b3). It can be observed that chain primitives do not intersect with each other. The convergence history of the optimisation is given in Fig. 16**Error! Reference source not found.**(c1)-(c3). For CPTO 3C4B, the optimisation takes 282 iterations to converge. The compliance of the final design is 21.37, while the volume of carbon fibre filament only reaches 49.12%. For CPTO 4C4B, the compliance converges to 19.41 after 300 iterations. Lastly, for CPTO 3C6B, it takes 173 iterations for the algorithm to complete the optimisation. The compliance of the final design is 17.09.

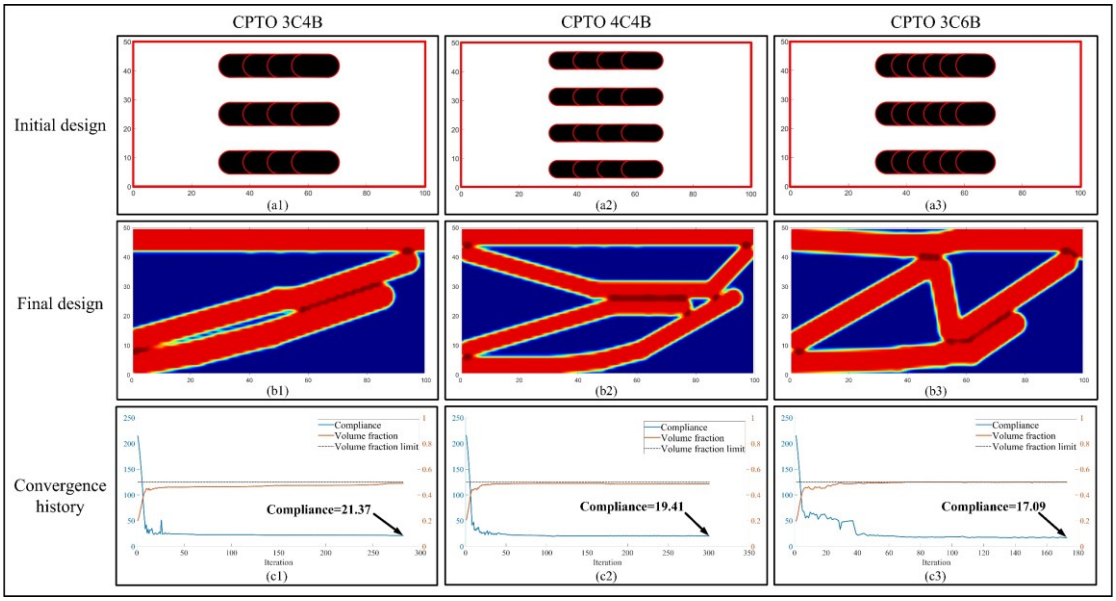

Fig. 16. Topology optimisation result of the cantilever case

Table 4 The chain primitive layouts for the cantilever case

Case	Number of chain primitives	Number of bar components in each chain
CPTO 3C4B	3	4
CPTO 4C4B	4	4
CPTO 3C6B	3	6

The printing paths of the optimised cantilevers are drawn in Fig. 17. Apparently, the carbon fibre filaments and PA6 fully occupy the respective areas, which indicates that *Phenomenon 1* is prevented in

the case study. Additionally, sharp corners less than 90° and loop-like paths do not exist in the printing paths, which means that *Phenomenon 2* is avoided.

The comparison of the mechanical performance of different cantilever designs is given in Fig. 18. The Y-axis denotes the stiffness of each optimised structure, which is computed by Eq. (35). Similar to the MBB case, CPTO-optimised structures show significantly higher stiffness while considering the manufacturing factors.

Comparing the mechanical performance of the structures designed by the CPTO method in the two cases of MBB and cantilever, the following conclusions can be drawn: for the CPTO method under the precondition of using relatively fewer chain primitives, it is to some extent beneficial to obtain better mechanical performance by increasing the number of bar components in each chain primitive appropriately. There may be two reasons for this phenomenon: (1) chains will avoid crossing over each other under the overlapping constraint. When the number of chain primitives in the design space increases, the active space of each chain will become smaller, thus hindering the optimisation algorithm from finding better solutions; (2) When the number of bar components included in the chain primitive is small, the freedom in the optimisation problem will also be relatively reduced, limiting the algorithm from finding the optimal solution.

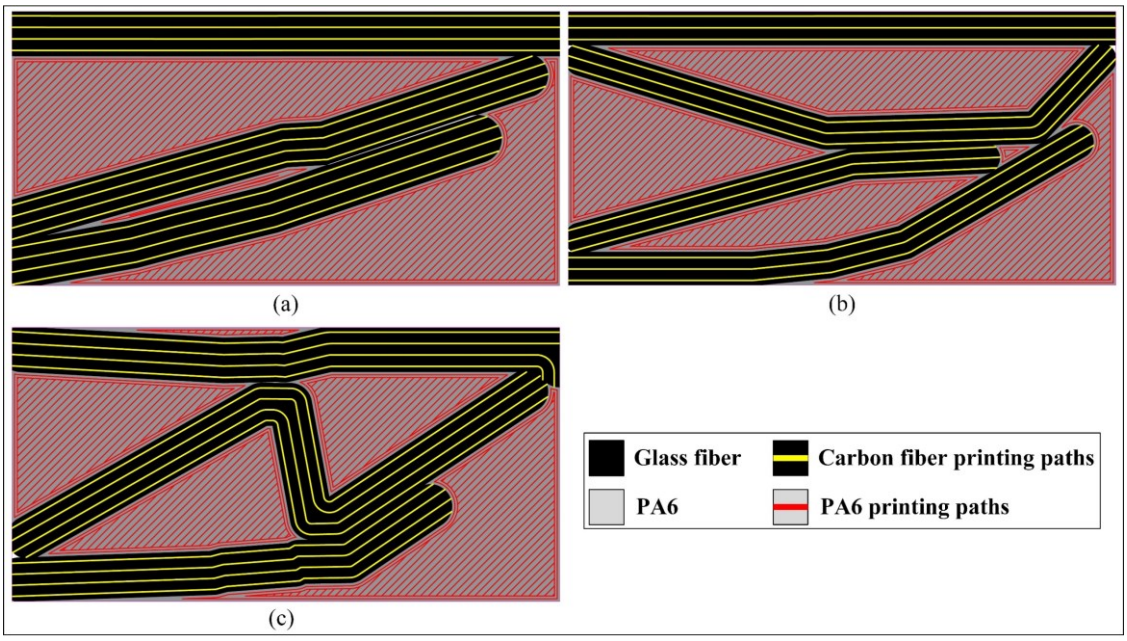

Fig. 17. Printing paths designed by the CPTO method

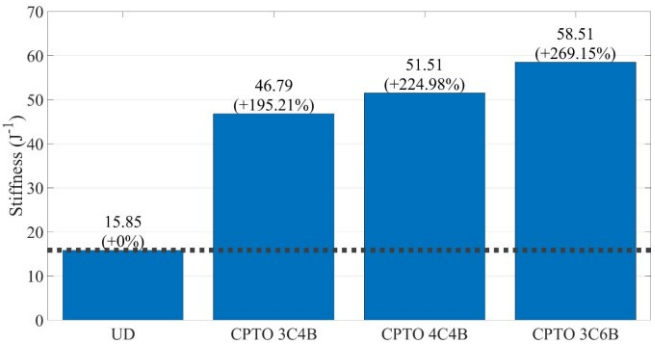

Fig. 18. Structural stiffness of cantilever beam based on different design methods.

3.3 Bridge

In the above case studies, the composite structures designed by the CPTO method exhibit considerable improvement of stiffness compared to UD structures with the same carbon fibre volume fractions. However, the advantages of the CPTO method in terms of printing path planning are not intuitively demonstrated in those cases. Thus, in the current case, a bridge is topologically optimised separately by the DCP and CPTO methods. The Offset method is utilised to design a printing path for the composite structure optimised by the DCP method. According to [23], the Offset method creates contours which are parallel to the boundary of the structure. First, the boundary of the structure is defined, then a parallel printing path is created at a prescribed distance (width of fibre filament). The next parallel printing path to the one created is placed again at the same distance. The process stops when a new parallel contour intersects a previously created one. The Offset method is chosen for comparison in this case study because of its relatively high robustness and infill rate. The boundary condition of the bridge is given in Fig. 19. The volume fraction of carbon fibre filament is 0.5.

Fig. 19 illustrates the pseudo density and orientation field of topology-optimised structures on the left side. On the other side, the voxel mesh models based on the actual 3D printing path are given, in which the black region refers to 3D printed carbon fibre epoxy filaments and the grey region refers to pure epoxy. The carbon fibre voxel mesh is embedded in the epoxy model. The voxel mesh models are generated by TexGen [44] and inputted into Abaqus for FEA. The workflow was also detailed in our former study [45].

The FEA result shows that the stiffness of the CPTO structure is 24.06% lower than that of the DCP+Offset structure. The relatively declined performance is due to the three manufacturing constraints

introduced in the CPTO method. The phenomenon was also seen in other researches focused on manufacturing [46-48].

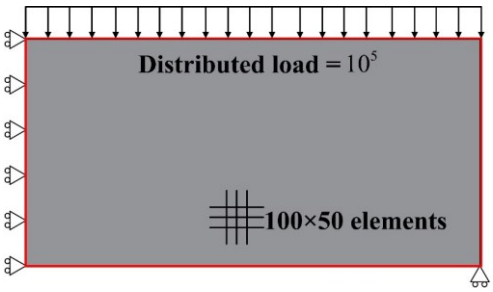

Fig. 19. Boundary condition of the bridge case

However, it must be emphasised that with the decrease in stiffness of the CPTO structure, the convenience of 3D printing also follows. According to [25], the curvature at each position in the 3D printing path is a significant parameter that can directly reflect the printing feasibility and quality. In Fig. 20, two histograms visually show the curvature of the Offset printing path and the CPTO printing path, respectively. The two different paths are divided evenly into 100 sections. The vertical axis of the histogram represents the maximum curvature value in each section, while the horizontal axis represents the position of the section relative to the starting point. The curvature of the CPTO printing path is relatively minor, which means its manufacturability is primarily enhanced, and there will be less significant bending of the fibre filaments during the 3D printing process, thus reducing the possibility of fibre breakage and distortion.

The minimum and maximum principal stress distributions of the two models are illustrated in Fig. 21. It can be seen that in the Offset model, there appears stress concentration and non-uniformity around the sharp corners (highlighted by black boxes), while the stress in the CPTO model is distributed more evenly. The phenomenon suggests that there may be more potential locations for fibre fracture in Offset composite structure.

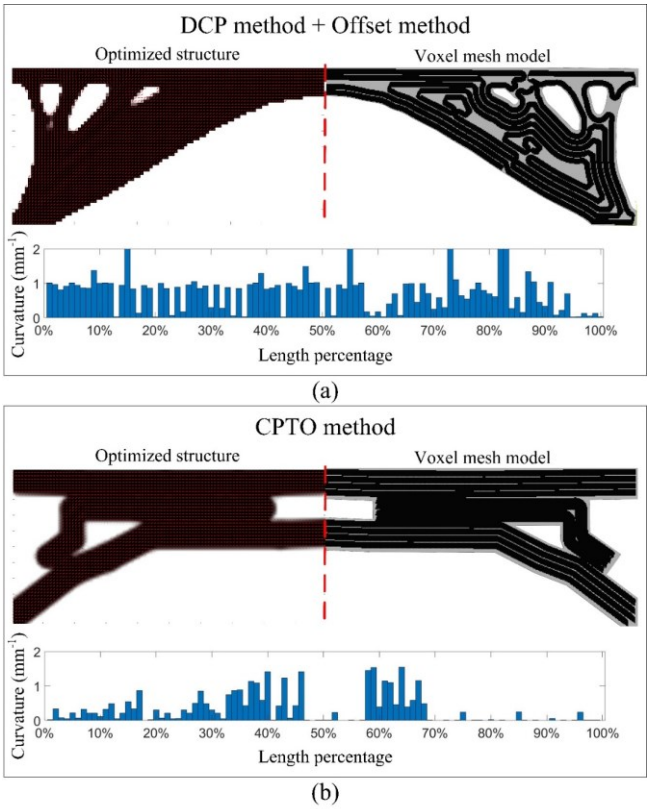

Fig. 20. Optimised structure, voxel mesh model, and curvature distribution of printing paths of different methods: (a) DCP+Offset and (b) CPTO.

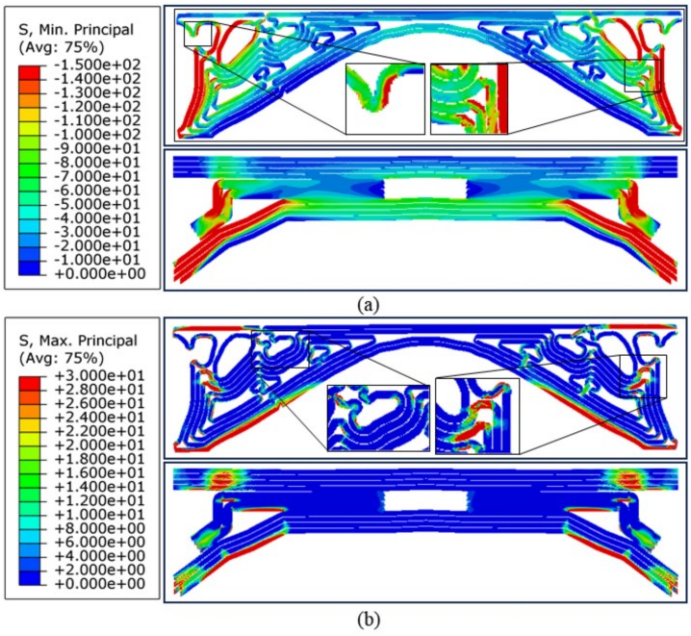

Fig. 21. Stress distribution in the printed filaments: (a) minimum principal stress and (b) maximum principal stress

More importantly, during the 3D printing process the loop-like printing paths generated by the Offset method cannot be printed directly, and they need to be truncated at specific locations and connected to

other loops. As for where to truncate to maximise the structural mechanical performance, there is still currently a lack of rigorous guidances. Therefore, the truncation position is usually artificially determined, introducing inevitable uncertainty factors into the actual mechanical performance. 3D printing experiments are also carried out to demonstrate the manufacturability of the optimised designs by the CPTO method. To this end, a Prusa i3 MK3s 3D printer without a filament cutting mechanism is used for printing the continuous fibre filament, as shown in Fig. 22(a). The nozzle temperature was set as 120 °C, the printing bed temperature was 20 °C, and the printing speed was 15 mm/min.

For the purpose of better observing the printing quality, only one layer was printed. The Offset sample is shown in Fig. 22(b). The boundary of the composite structure is drawn in red polylines. As depicted above, the Offset method cannot achieve a 100% infill rate in most cases, especially after the modification to fit the demand of 3D printing. The area not infilled by the CCF/epoxy filament, but by pure epoxy, is highlighted in blue. The epoxy resin-rich area will inevitably deteriorate the mechanical performance and possibly be the starting region of cracks, according to our previous research [49].

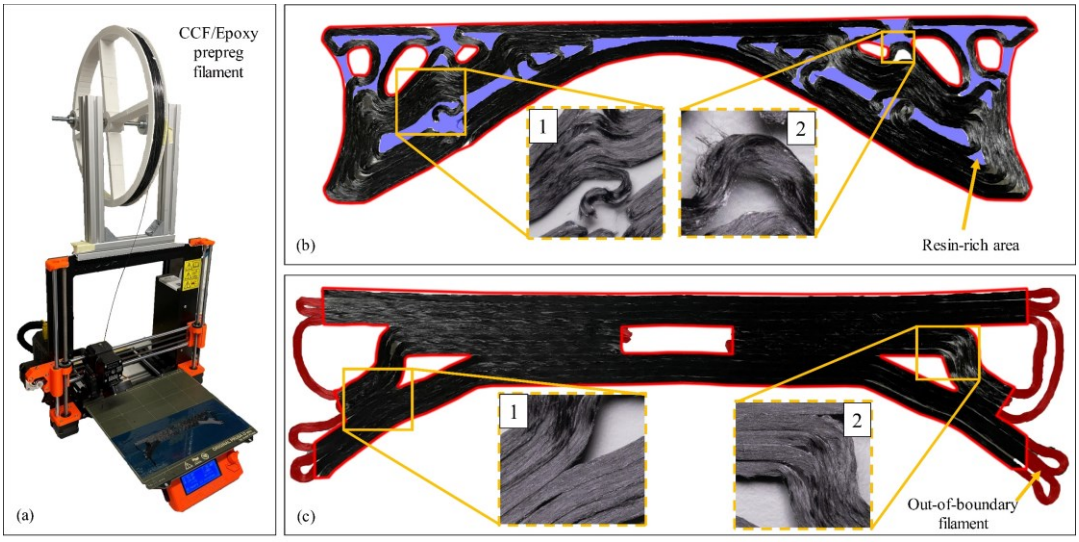

Fig. 22. (a) Prusa i3 MK3s 3D printer, (b) 3D printed Offset structure and (c) 3D printed CPTO structure

Additionally, two representative regions are highlighted by the orange box. In the first region, severe misalignment and twisting of fibre filaments can be observed at the end of the printing path; in the second area, obvious fibre breakage can be seen at the edges of the CCF/epoxy filament. The undesirable defects can be observed throughout the whole sample, as the offset printing path is composed by numerous sharp

corners. Furthermore, given the presence of stress concentration around sharp corners as illustrated in Fig. 21, the aforementioned manufacturing defects will potentially lead to early fractures in the printed composite.

The CPTO sample is shown in Fig. 22(c). The filament outside the structural boundary lines is highlighted in red, which are cut off during the post-processing of the sample. Like the Offset sample, two typical regions are also highlighted with orange boxes in the image. In the first region, similar to most other parts of the CPTO sample, the distribution of filaments is very smooth without manufacturing defects. The second area is the location with the highest curvature of filaments in the CPTO sample, where some bending of filaments can be observed, but no noticeable fibre misalignment and filament twist are found. Furthermore, no gaps or overlaps between filaments are found in Fig. 22(c), indicating that the printing path designed by the CPTO method can indeed avoid the undesirable phenomena listed in Table 1 during the actual 3D printing process.

4. Conclusions

In the traditional topology optimisation and printing path design frameworks, three phenomena are hard to avoid: (1) The structures are infilled not according to the material used in the topology optimisation, (2) The printing path is composed of loops and/or sharp corners and (3) The printing paths overlap with each other. The phenomena all contribute to the mechanical performance discrepancy between the 3D-printed composite structure and its corresponding numerical design. To optimise the composite structures and design 3D printing paths while avoiding the above phenomena, in this study, a novel Chain Projection Topology Optimisation method (CPTO) for the 3D printing of composite structures is developed using chain-like primitives. In CPTO, the widths of chains are set as multiple times of the printed fibre filament width, ensuring the printing paths of fibre filaments to be generated along the orientation of chains. Furthermore, constraints of overlapping and angles between adjacent bars in the primitive chain are introduced to the optimisation, enabling the manufacturability of the designs from the CPTO optimisation.

An MBB beam, a cantilever beam, and a bridge case are numerically demonstrated to prove the effectiveness of the CPTO method. The optimisation results show that the mechanical performance of the designs from the CPTO method are close to the sequential optimisation result while much better facilitating the 3D printing process. The optimised designs are further 3D printed using CCF/epoxy

filament as reinforcement, which shows that the three undesirable phenomena are prevented in the CPTO method. The numerical case studies and the 3D printing validation proved that the CPTO method is able to find a composite structure with relatively good stiffness while ensuring it is easy to be 3D printed and contains less potential microscopic defects in the printed fibre filaments.

Acknowledgment

The authors would like to acknowledge financial support from Royal Society and National Science Foundation of China for the International Exchanges Scheme (IEC/NSFC/170418), National Science Foundation of China (Grant No. 51975199 and Grant No. 12302260), Natural Science Foundation of Hunan Province (Grant No. 2022JJ30004). Shuai Wang would like to acknowledge the support from China Scholarship Council (Grant No. 202006130128).

References

[1] F.C. Campbell Jr, Manufacturing processes for advanced composites, elsevier2003.
[2] A. Riveiro, F. Quintero, F. Lusquiños, J. Del Val, R. Comesaña, M. Boutinguiza, J. Pou, Experimental study on the CO2 laser cutting of carbon fiber reinforced plastic composite, Composites Part A: Applied Science and Manufacturing 43(8) (2012) 1400-1409.
[3] M. Li, G. Gan, Y. Zhang, X. Yang, Thermal damage of CFRP laminate in fiber laser cutting process and its impact on the mechanical behavior and strain distribution, Archives of Civil and Mechanical Engineering 19 (2019) 1511-1522.
[4] J.P. Davim, P. Reis, Study of delamination in drilling carbon fiber reinforced plastics (CFRP) using design experiments, Composite structures 59(4) (2003) 481-487.
[5] J.P. Davim, P. Reis, Drilling carbon fiber reinforced plastics manufactured by autoclave—experimental and statistical study, Materials & design 24(5) (2003) 315-324.
[6] N. Li, Y. Li, S. Liu, Rapid prototyping of continuous carbon fiber reinforced polylactic acid composites by 3D printing, Journal of Materials Processing Technology 238 (2016) 218-225.
[7] M. Mohammadizadeh, A. Imeri, I. Fidan, M. Elkelany, 3D printed fiber reinforced polymer composites-Structural analysis, Composites Part B: Engineering 175 (2019) 107112.
[8] A.V. Azarov, F.K. Antonov, M.V. Golubev, A.R. Khaziev, S.A. Ushanov, Composite 3D printing for the small size unmanned aerial vehicle structure, Composites Part B: Engineering 169 (2019) 157-163.
[9] H.P. Jia, C.D. Jiang, G.P. Li, R.Q. Mu, B. Liu, C.B. Jiang, Topology optimization of orthotropic material structure, Materials Science Forum, Trans Tech Publ, 2008, pp. 978-989.
[10] T. Nomura, E.M. Dede, J. Lee, S. Yamasaki, T. Matsumori, A. Kawamoto, N. Kikuchi, General topology optimization method with continuous and discrete orientation design using isoparametric projection, International Journal for Numerical Methods in Engineering 101(8) (2015) 571-605.
[11] Y. Luo, W. Chen, S. Liu, Q. Li, Y. Ma, A discrete-continuous parameterization (DCP) for concurrent optimization of structural topologies and continuous material orientations, Composite Structures 236 (2020) 111900.
[12] Z. Qiu, Q. Li, Y. Luo, S. Liu, Concurrent topology and fiber orientation optimization method for fiber-reinforced composites based on composite additive manufacturing, Computer Methods in Applied Mechanics and Engineering 395 (2022) 114962.
[13] O. Sigmund, A 99 line topology optimization code written in Matlab, Structural and multidisciplinary optimization 21(2) (2001) 120-127.
[14] M.P. Bendsoe, O. Sigmund, Topology optimization: theory, methods, and applications, Springer Science & Business Media2003.
[15] E. Andreassen, A. Clausen, M. Schevenels, B.S. Lazarov, O. Sigmund, Efficient topology optimization in MATLAB using 88 lines of code, Structural and Multidisciplinary Optimization 43(1) (2011) 1-16.

[16] J. Stegmann, E. Lund, Discrete material optimization of general composite shell structures, International Journal for Numerical Methods in Engineering 62(14) (2005) 2009-2027.
[17] Y. Xu, Y. Gao, C. Wu, J. Fang, Q. Li, Robust topology optimization for multiple fiber-reinforced plastic (FRP) composites under loading uncertainties, Structural and Multidisciplinary Optimization 59(3) (2019) 695-711.
[18] D.R. Jantos, K. Hackl, P. Junker, Topology optimization with anisotropic materials, including a filter to smooth fiber pathways, Structural and Multidisciplinary Optimization (2020) 1-20.
[19] A. Moter, M. Abdelhamid, A. Czekanski, Direction-oriented stress-constrained topology optimization of orthotropic materials, Structural and Multidisciplinary Optimization 65(6) (2022) 1-17.
[20] E. Sales, T.-H. Kwok, Y. Chen, Function-aware slicing using principal stress line for toolpath planning in additive manufacturing, Journal of Manufacturing Processes 64 (2021) 1420-1433.
[21] Z. Hou, X. Tian, J. Zhang, Z. Zheng, L. Zhe, D. Li, A.V. Malakhov, A.N. Polilov, Optimization design and 3D printing of curvilinear fiber reinforced variable stiffness composites, Composites Science and Technology 201 (2021) 108502.
[22] H. Zhang, D. Yang, Y. Sheng, Performance-driven 3D printing of continuous curved carbon fibre reinforced polymer composites: A preliminary numerical study, Composites Part B: Engineering 151 (2018) 256-264.
[23] V.S. Papapetrou, C. Patel, A.Y. Tamijani, Stiffness-based optimization framework for the topology and fiber paths of continuous fiber composites, Composites Part B: Engineering 183 (2020) 107681.
[24] R.R. Fernandes, N. van de Werken, P. Koirala, T. Yap, A.Y. Tamijani, M. Tehrani, Experimental Investigation of Additively Manufactured Continuous Fiber Reinforced Composite Parts with Optimized Topology and Fiber Paths, Additive Manufacturing (2021) 102056.
[25] T. Wang, N. Li, G. Link, J. Jelonnek, J. Fleischer, J. Dittus, D. Kupzik, Load-dependent path planning method for 3D printing of continuous fiber reinforced plastics, Composites Part A: Applied Science and Manufacturing 140 (2021) 106181.
[26] R. Matsuzaki, T. Nakamura, K. Sugiyama, M. Ueda, A. Todoroki, Y. Hirano, Y. Yamagata, Effects of set curvature and fiber bundle size on the printed radius of curvature by a continuous carbon fiber composite 3D printer, Additive Manufacturing 24 (2018) 93-102.
[27] H. Zhang, J. Chen, D. Yang, Fibre misalignment and breakage in 3D printing of continuous carbon fibre reinforced thermoplastic composites, Additive manufacturing 38 (2021) 101775.
[28] M.Y. Wang, X. Wang, D. Guo, A level set method for structural topology optimization, Computer methods in applied mechanics and engineering 192(1-2) (2003) 227-246.
[29] V.J. Challis, A discrete level-set topology optimization code written in Matlab, Structural and multidisciplinary optimization 41(3) (2010) 453-464.
[30] J. Liu, H. Yu, Concurrent deposition path planning and structural topology optimization for additive manufacturing, Rapid Prototyping Journal (2017).
[31] J. Liu, J. Huang, J. Yan, L. Li, S. Li, Full sensitivity-driven gap/overlap free design of carbon fiber-reinforced composites for 3D printing, Applied Mathematical Modelling 103 (2022) 308-326.
[32] Z. He, M. Tehrani, A.Y. Tamijani, Strength-based concurrent shape and fiber path optimization of continuous fiber composites, Computer Methods in Applied Mechanics and Engineering 399 (2022) 115414.
[33] H. Cheng, N. Kikuchi, Z. Ma, An improved approach for determining the optimal orientation of orthotropic material, Structural optimization 8(2) (1994) 101-112.
[34] H. Gea, J. Luo, On the stress-based and strain-based methods for predicting optimal orientation of orthotropic materials, Structural and Multidisciplinary Optimization 26(3-4) (2004) 229-234.
[35] M. Lan, D. Cartié, P. Davies, C. Baley, Influence of embedded gap and overlap fiber placement defects on the microstructure and shear and compression properties of carbon–epoxy laminates, Composites Part A: Applied Science and Manufacturing 82 (2016) 198-207.
[36] J. Norato, B. Bell, D.A. Tortorelli, A geometry projection method for continuum-based topology optimization with discrete elements, Computer Methods in Applied Mechanics and Engineering 293 (2015) 306-327.
[37] H. Smith, J.A. Norato, A MATLAB code for topology optimization using the geometry projection method, Structural and Multidisciplinary Optimization (2020) 1-16.
[38] H. Smith, J.A. Norato, Topology optimization with discrete geometric components made of composite materials, Computer Methods in Applied Mechanics and Engineering 376 (2021) 113582.
[39] H. Smith, J. Norato, Topology optimization of structures made of fiber-reinforced plates, Structural and Multidisciplinary Optimization 65(2) (2022) 58.

[40] J. Greifenstein, E. Letournel, M. Stingl, F. Wein, Efficient spline design via feature-mapping for continuous fiber-reinforced structures, Structural and Multidisciplinary Optimization 66(5) (2023) 99.
[41] M. Heidari-Rarani, M. Rafiee-Afarani, A. Zahedi, Mechanical characterization of FDM 3D printing of continuous carbon fiber reinforced PLA composites, Composites Part B: Engineering 175 (2019) 107147.
[42] H. Shiratori, A. Todoroki, M. Ueda, R. Matsuzaki, Y. Hirano, Mechanism of folding a fiber bundle in the curved section of 3D printed carbon fiber reinforced plastics, Advanced Composite Materials 29(3) (2020) 247-257.
[43] K. Svanberg, The method of moving asymptotes—a new method for structural optimization, International journal for numerical methods in engineering 24(2) (1987) 359-373.
[44] H. Lin, L.P. Brown, A.C. Long, Modelling and simulating textile structures using TexGen, Advanced Materials Research, Trans Tech Publ, 2011, pp. 44-47.
[45] H. Zhang, S. Wang, K. Zhang, J. Wu, A. Li, J. Liu, D. Yang, 3D printing of continuous carbon fibre reinforced polymer composites with optimised structural topology and fibre orientation, Composite Structures 313 (2023) 116914.
[46] E. Fernández, C. Ayas, M. Langelaar, P. Duysinx, Topology optimisation for large-scale additive manufacturing: generating designs tailored to the deposition nozzle size, Virtual and Physical Prototyping 16(2) (2021) 196-220.
[47] C. Wang, X. Qian, Simultaneous optimization of build orientation and topology for additive manufacturing, Additive Manufacturing 34 (2020) 101246.
[48] W. Zhang, W. Zhong, X. Guo, An explicit length scale control approach in SIMP-based topology optimization, Computer Methods in Applied Mechanics and Engineering 282 (2014) 71-86.
[49] S. Wang, H. Zhang, A. Li, J.A.A. Qayyum, Y. Wang, Z. He, J. Liu, D. Yang, A modified equally-spaced method (MEQS) for fibre placement in additive manufacturing of topology-optimised continuous carbon fibre-reinforced polymer composite structures, Composite Structures (2024) 117998.